

RESEARCH

Open Access



Thunderstorm identification algorithm research based on simulated airborne weather radar reflectivity data

Xu Wang¹, Rui Liao¹, Jing Li², Jianxin He¹, Guoqiang Wang², Zili Xu² and Haijiang Wang^{1*} 

Abstract

In the past few decades, radar reflectivity data have been widely used in thunderstorm identification research. Many thunderstorm identification algorithms for ground-based weather radar have been developed. But for airborne weather radar, due to the relative scarcity of data, the thunderstorm identification research is insufficient and there are still few effective identification methods. Airborne weather radar has the realization capability of close-range detection, but most existing airborne weather radars do not have scanning capability. This paper proposes an airborne weather radar volume scan mode, under which there is a total of 31 sector scans at 31 elevations in a volume scan. And a reflectivity data simulation model of the airborne weather radar is established based on this scan strategy, then the ground-based X-band radar reflectivity data are used as input to obtain the simulated X-band airborne radar reflectivity data. Moreover, this paper studies a thunderstorm identification algorithm for the X-band airborne radar with the proposed scan mode. An improved SCI (storm cell identification) algorithm is proposed on the basis of the traditional SCI algorithm which is applicable to S-band ground-based weather radar. The results of thunderstorm identification carried out on the simulated airborne radar data show that the algorithm can effectively identify the thunderstorm cells in the mature stage and the developing stage.

Keywords: Airborne weather radar, Volume scan, Reflectivity, Thunderstorm identification, SCI algorithm

1 Introduction

As an extension of weather radar, airborne weather radar can detect weather system at a close range, making up for the inflexibility of ground-based radar and scant meteorological information with low resolution of space-based radar caused by the long-distance [1]. It is very difficult for civil aviation aircraft to grasp the meteorological dynamics on air route just rely on the information of ground weather stations. The airborne weather radar can detect the weather conditions in front of the flight in real time during flying and feedback the information, such as the location and intensity of a meteorological target, to the pilot, which is conducive to choose safe routes to avoid thunderstorm and other weather threatening aviation safety. Several countries started to do researches on airborne

atmospheric sounding system earlier (e.g., USA, Britain, France) [2]. Here are some representative airborne weather radars and the information shown in Table 1.

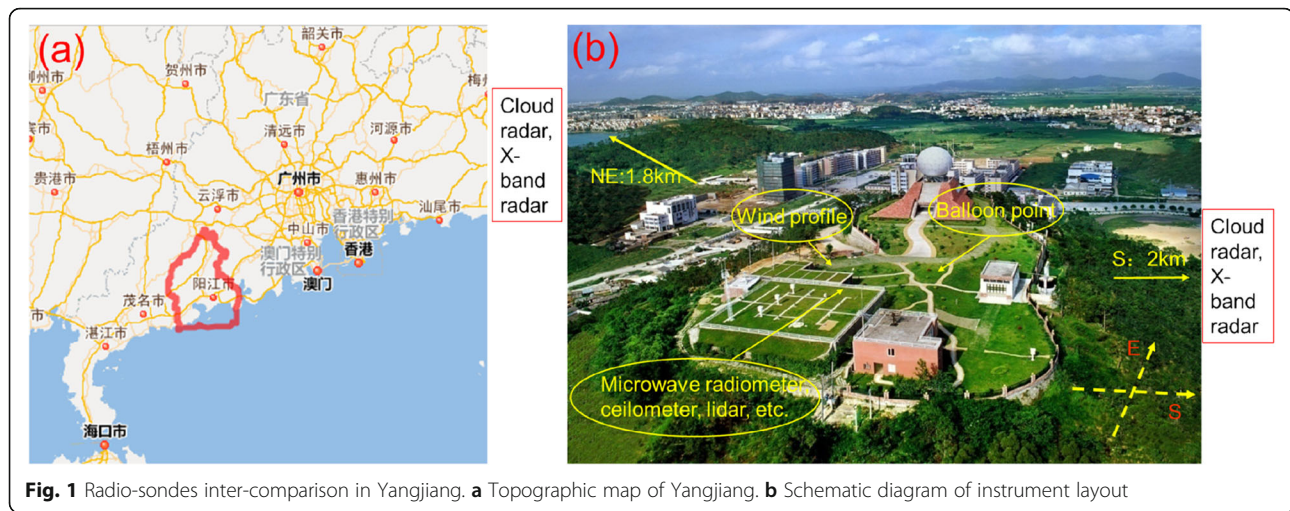
Except that the Spider is capable of limited cross-scanning, most of the above radars have no scanning capability. This paper proposes an airborne weather radar with volume scanning mode, something similar to WSR-88D (Weather Surveillance Radar 1988 Doppler in America) radar. Beginning from the lowest elevation, the radar scans the sector in front of the aircraft with the maximum detection distance as the radius, and raises its antenna by 1° to scan the next elevation every time ends the current elevation scan. A volume scan data will be formed until the highest elevation angle scan ends. In this way, the radar will be able to obtain enough high resolution echo information of the space ahead of flight. It may play an important role for the future meteorological research especially severe weather such as thunderstorms, which contributes to improving weather monitoring and ensuring flight safety.

* Correspondence: whj@cuit.edu.cn

¹Key Laboratory of Atmospheric Sounding of China Meteorological Administration, Electronic Engineering College of Chengdu University of Information Technology, Chengdu 610225, Sichuan, China
Full list of author information is available at the end of the article

Table 1 Information of some representative airborne weather radar

Radar	Country/company	Wavelength	Scan mode	Application
ELDORA(ASTRATA)	USA and France	3 cm (X-band)	Rotary scanning of two antennas (forward and backward) with an angle of 18.5°	Convective storm detection with high resolution
WXR-2100	Rockwell-Collins	3.1 cm (X-band)	Emits two beams with slight offset in the vertical (pitch) direction	Detecting convective clouds that threaten aircraft safety
CRS	Goddard Space Flight Center(NASA)	3.2 mm (W-band)	Scanning with a two-axis gimbal hanger(airborne)RHI scanning(ground-based)	Cloud measurement, especially cirrus
ACR	UMass and JPL(NASA)	3 mm (W-band)	Detect vertically downwards or upwards	Weak precipitation and snowfall
Spider	Japan	3 mm (W-band)	Scanning in the direction of the track from −40° to +95°	Cloud measurement



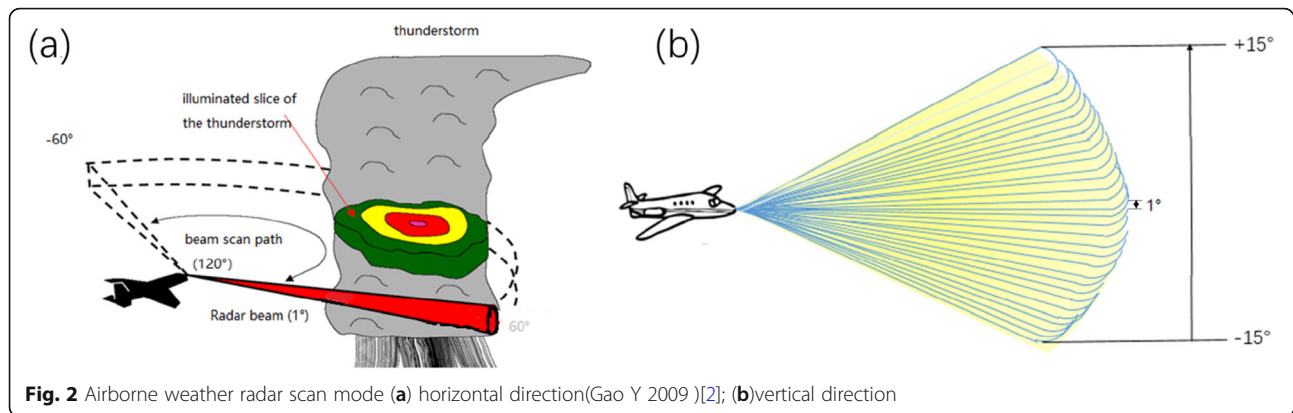
Thunderstorm, refers to the deep moist convection phenomenon and accompanied by lightning, thunder, rainstorm, gale, turbulence, hail and etc. as a rule, is an important component of disastrous weather in China (Yu X et al. 2012) [3]. Thunderstorms threaten aviation safety and affect aviation operations. According to the statistics of civil aviation organizations, the accidents directly and indirectly caused by thunderstorms account for more than 50% of all the flight accidents caused by meteorological reasons (Wei X et al. 2013 and Zhang X 2011) [4, 5]. Improving the ability to identify thunderstorms is of great significance for forecasting and early warning and further reducing risks and losses. Thunderstorms are characterized by short life cycle, small range, and strong destructive power. Since ground-based radar is far away from storms and has limited detection accuracy, airborne radar has become an effective means of real-time detection and warning with its high spatial-temporal resolution.

At present, threshold segmentation method [6–10], algorithm based on image processing [11], Gaussian mixture model [12], cluster analysis [13], and machine learning [14–22] have been used for convective target identification. Especially, the method based on machine learning is widely used in radar meteorology and hydrology research and in recent years, such as

fuzzy logic, decision tree and neural network, etc. Through the identification of hydraulic condensate particles (e.g., Dolan B 2008 and Liu Y 2014) [18–20] and the inversion of soil moisture (e.g., Jing Liang et al. 2017 and 2018) [21, 22], the law of solid-liquid-gas three-state transformation in hydrological process is explored, which provides hydrological basis for engineering construction management and human activities. But the results of the machine learning algorithm depend on the accuracy of the input data, so it is not suitable for the simulation data in this paper for the time being. However, threshold segmentation is a mature technology among the methods mentioned before. In the past few decades, there are many innovation researches based on threshold segmentation proposed. For example, Dixon et al. (1993) proposed TITAN (Thunderstorm Identification, Tracking, Analysis, and Now Casting) algorithm to identify convective storms using a single reflectivity threshold of 30dBZ [6]. Han et al. (2009) made some improvements on TITAN algorithm, called ETITAN, using multiple thresholds to identify convective storms, solving the false segmentation phenomenon when storms are separated by introducing corrosion and expansion in mathematical morphology [7]. Wang L et al. (2017) established a simulation model for airborne weather radar and used improved region segmentation method and TITAN algorithm to identify severe storm [8]. Kyznarová et al. (2009) used 44 dBZ as a threshold to identify convection cell [9]. Johnson et al. (1998) proposed the SCIT algorithm (the storm cell identification and tracking algorithm) which regards convective targets as 3D structures and uses seven reflectivity thresholds to identify severe storms through three steps of identifying cell segments, cell components, and storm cell successively [10]. The algorithm was developed for use on WSR-88D in

Table 2 X-band ground-based radar scan parameters

Parameter	Value
Range resolution (m)	62.5
Azimuth range (°)	0~360
Azimuth resolution (°)	360/700
Maximum detection range (km)	62.5
Elevation number (layer)	9
Elevation (°)	1.5, 2.4, 3.4, 4.5, 6, 7.5, 9.9, 14.6, 19.5



America, and later on a new generation of Doppler weather radar (CINRAD) in China. In the past few years, many Chinese researchers have made relevant researches on severe convective weather based on SCIT or its improvement algorithm (e.g., Huang L 2014 and Lu D 2015) [23–26]. It is evidenced that SCIT algorithm has higher recognition rate for convection cell with high reflectivity intensity, as it can correctly identify 68% storms with maximum reflectivity factor over 40 dBz and 96% storms with maximum reflectivity factor over 50 dBz (Han L et al. 2007) [26]. Because of convection cell's growth and dissipating, the multi-threshold method has a better identification effect than a single threshold. Ultimately, this paper conducts a study on the thunderstorm identification algorithm based on SCI algorithm, storm cell identification part of SCIT algorithm.

2 Methods

This experiment mainly applies the simulated airborne weather radar reflectivity to achieve thunderstorm identification, thus realizing the cross-validation of simulation data and identification algorithm. Therefore, this section introduces the establishment of the reflectivity data model of airborne weather radar and the research and verification of the thunderstorm identification algorithm.

2.1 Airborne radar data simulation

As the parameter selection of the simulation model is determined by the data format of the input data and the output data, the data format is closely related to the scan mode of the radar. Therefore, this section introduces the radar scan method of data source and target data and the method of establishing a simulation model respectively.

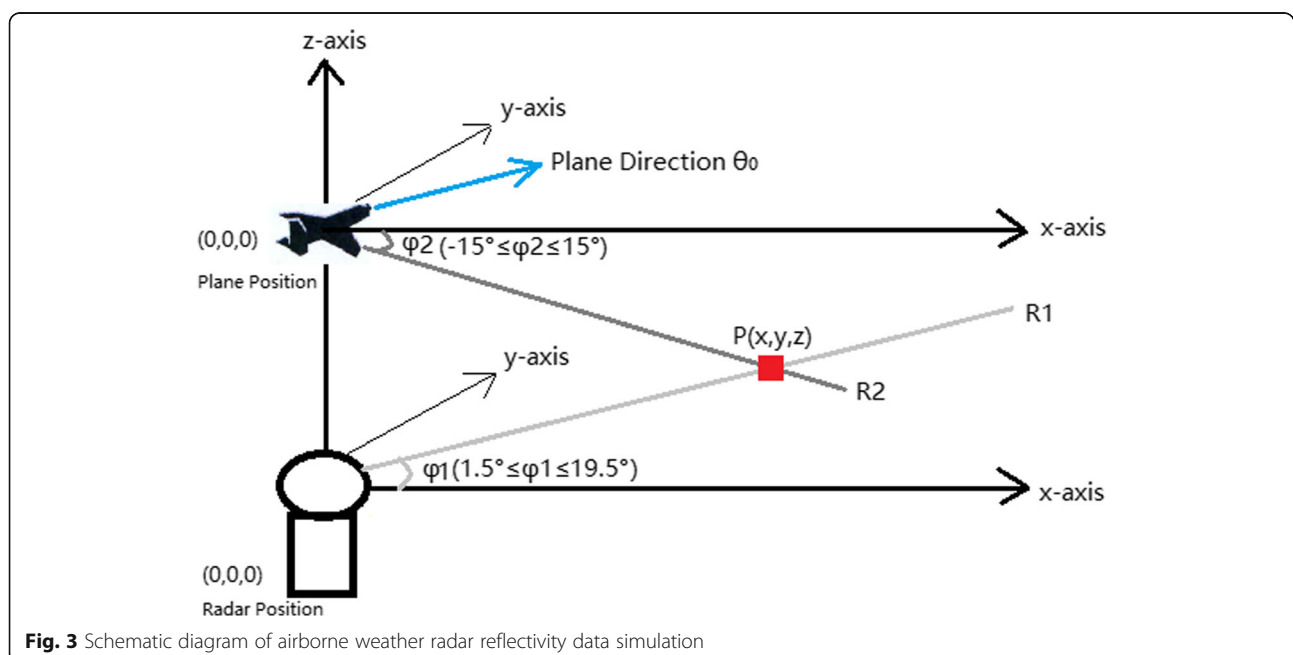


Table 3 Simulated airborne weather radar scan parameters

Parameter	Value
Maximum detection range (km)	60
Range resolution (km)	0.1
Azimuth range (°)	120(± 60)
Azimuth resolution (°)	1
Elevation resolution (°)	1
Elevation range (°)	− 15~ + 15

2.1.1 Data source of simulation

Ground-based weather radar data used to simulate in this paper is from one X-band radar of Yangjiang 8th International Radio-sonde Inter-comparison held successfully by WMO from 12 July to 1 August 2010 [27]. Yangjiang, a prefecture-level city under the jurisdiction of Guangdong Province, locates on the southwest coast of Guangdong Province and is the direct hinterland of the Pearl River Delta and the frontier of western Guangdong facing the Pearl River Delta (Fig. 1a). The topography is mainly low mountains and hills, which is a subtropical monsoon climate zone with obvious marine climate. Convective weather is frequent in July and August here, which is favorable for observation. In this experiment, 20 kinds of remote sensing instruments including one S-band weather radar, two X-band dual-polarization radars, and two millimeter-wave radars were used to carry out a series of observation experiments (Fig. 1b). This experiment realizes continuous cooperative observation of one target, which is conducive to achieving the purpose of sounding observation comparison of different observation equipment.

For the reason that X-band radar is small in size, short in detection distance and low in cost, it is

convenient to be airborne. We select one X-band radar data of convective cells observed on 20 July as the source of simulation. And its scan parameters are shown in Table 2.

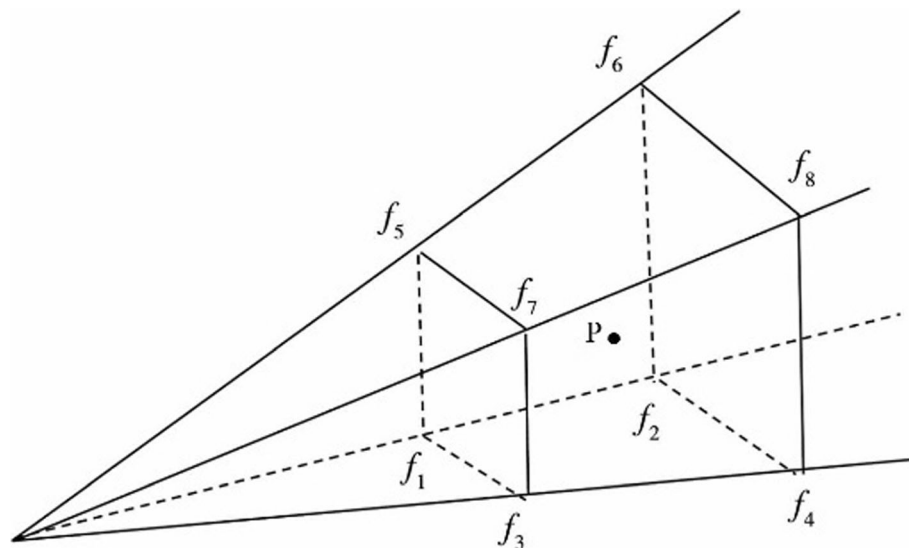
2.1.2 Airborne weather radar scan mode

The airborne weather radar proposed in this paper begins scanning from the lowest elevation -15° . The scanning area is a fan-shaped area with azimuth ranges from -60 to 60° centering on aircraft heading and a radius of 60 km (Fig. 2a). The radar raises its antenna angle by 1° and scans the next elevation after ends the current elevation scan. And it will form a volume scan data when the last elevation 15° is the end of scanning (Fig. 2b).

The parameters of the scan mode are shown in Table 3. It can be known that there are 31 elevation scans in a volume, 120 radials per elevation scan and 600 sample volumes per radial scan. Therefore, every volume scan data has totaling 2,232,000 sample volumes. By further calculation, this airborne weather radar has a maximum vertical depth of 31 km at the range of 60 km ahead of the flight altitude approximately. If the radar is in a good position to the thunderstorm, it will obtain more detailed echo information of storms, and even the entire thunderstorm with a small scale.

2.1.3 Method of simulation

As Fig. 3 shows, the X-band ground-based radar station is the coordinate center, a plane carrying on the airborne weather radar is set to fly at the altitude H (set as 10 km) above the radar station vertically and its heading is θ_0 . Regardless of the impact of the aircraft's flight speed

**Fig. 4** Schematic diagram of 8-point interpolation (Lv B et al. 2016) [28]

on the radar detection data, meaning that the aircraft and the ground-based radar remain relatively stationary during the process of detection, the data obtained by the airborne radar should be basically consistent with the ground-based radar. According to the scanning mode introduced in section 2.2, the airborne weather radar scans at elevation ϕ_2 which range from -15 to 15° , respectively ($\phi_{2\max}$ means 15°) and scans the sector with left and right a maximum azimuth of 60° centered on the heading and a maximum detection range of 60 km in every elevation scan. And there are total 2,232,000 sample volumes in a volume scan data. Assuming P is the center of a sample volume of the data, if airborne radar reflectivity data is converted to rectangular coordinates, the point $P(x, y, z)$ should meet Eqs. (1) and (2).

$$\begin{cases} -60 \leq x \leq 60 \\ -60 \leq y \leq 60 \\ 0 \leq z \leq h + 60 * \sin \phi_{2\max} \end{cases} \quad (1)$$

$$\begin{cases} 0 \leq \sqrt{x^2 + y^2} \leq 60 \\ \theta_0 - 60 \leq \arctan\left(\frac{x}{y}\right) \leq \theta_0 + 60 \\ z = h + \sqrt{x^2 + y^2} \times \tan(\phi_2), -15 \leq \phi_2 \leq 15 \end{cases} \quad (2)$$

The reflectivity data model of airborne weather radar can be established by the above two formulas. However, only those points within the X-band scanning range can be calculated from the X-band radar data. ϕ_1 is the elevation angle of point P relative to

the horizontal plane, and only the points satisfying Eq. (3) could get the value of the reflectivity factor.

$$\begin{cases} z \geq 0 \\ 1.5 \leq \phi_1 \leq 19.5 \end{cases} \quad (3)$$

The reflectivity data of point P can be obtained by 8-point adaptive Barnes interpolation [28, 29]. Find the two elevations of the X-band ground-based radar closest to point P , the two radials closest to point P in each elevation angle and the two sample volumes closest to point P in every radial, eight sample volumes in total as $f_1 \sim f_8$ in Fig. 4. Set the index of these sample volumes is i . Through the known reflectivity Z_i and the information including the distance to the radar station R , the azimuth θ , the elevation ϕ_1 of $f_i(R_i, \theta_i, \phi_{1i})$ and $P(R_P, \theta_P, \phi_P)$, the reflectivity of point P Z_P can be calculated by Eq. (4).

$$\begin{cases} w = \exp\left(-\frac{(R_i - R_P)^2}{K_r^2} - \frac{(\theta_i - \theta_P)^2}{K_\theta^2} - \frac{(\phi_{1i} - \phi_P)^2}{K_\phi^2}\right) \\ Z_P = \frac{\sum_{i=1}^N Z_i \times w}{\sum_{i=1}^N w} \end{cases} \quad (4)$$

Here, w is weight coefficient of radar raw data sampling point, K_r , K_θ , and K_ϕ are smoothing parameters of the radial distance, azimuth, and elevation direction and respectively take 1.0, 0.67, and 0.67 in this paper, N is the total number of sample volumes in the area of

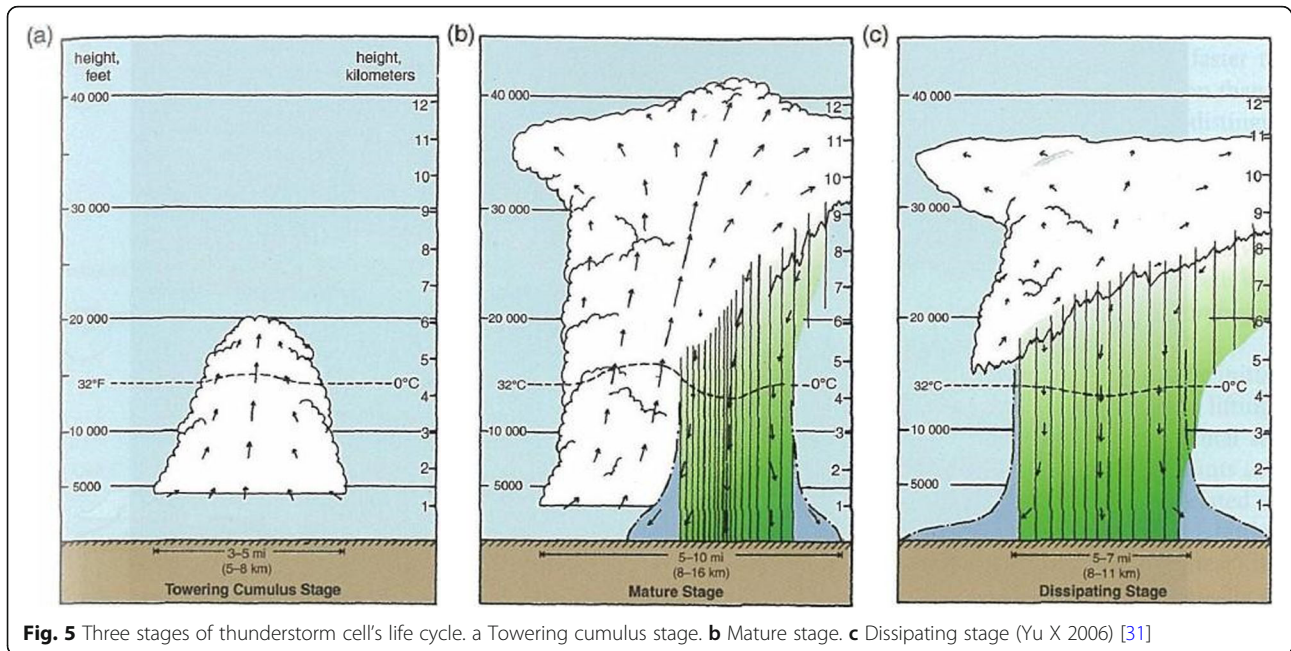


Table 4 Thresholds of cell segment search

Threshold	Meaning	Default value
Reflectivity(dBZ)	A set of minimum effective reflectivity which the reflectivity factor of a sample volume must meet or exceed to be included in a cell segment	25, 30, 35, 40, 45, 50, 55
Dropout reflectivity difference (dBZ)	The difference below threshold (reflectivity) in effective reflectivity that a sample volume may still be included in a cell segment	5
Dropout count(unit)	The maximum number of contiguous sample volumes with a reflectivity factor less than the threshold (reflectivity) by less than or equal to the threshold (dropout reflectivity difference) that may be included in a cell segment	2
Segment length (km)	Set of minimum lengths of a component for each reflectivity threshold	1

influence of the reflectance value and is taken as 8 (Huang Y et al. 2008) [29]. When all the sample volumes of the airborne weather radar reflectivity data are judged and calculated by the above method, a complete reflectivity volume scan data of the airborne weather radar can be finally obtained.

2.2 Thunderstorm identification

This section first introduces the life process of thunderstorms and their radar echo characteristics, which provides a theoretical basis for subsequent verification of thunderstorm identification results. Then the thunderstorm identification algorithm is introduced in detail, including the thunderstorm identification process, parameter selection, and the calculation method of key attributes.

2.2.1 Radar echo characteristics of thunderstorms

Convection cell is a cumulonimbus tower with a horizontal scale ranging from 1 to 2 km to a cumulonimbus system with dozens of kilometers. Convection cell

is defined as a continuous region where reflectivity intensity greater than 45 dBZ on the radar echo map. Thunderstorm cell is a system composed of a convection cell with a horizontal range from 10 km to tens of kilometers and a vertical structure that can extend to the whole troposphere.

As Fig. 4 shows, the life span of the thunderstorm cell can be roughly divided into three stages: towering cumulus stage, mature stage, and dissipating stage (Byers and Braham 1948) [30]. The towering cumulus stage is also called the development stage where there is a consistent updraft through the whole cloud and the cloud column develops upward (Fig. 5a). First of all, the radar echo of the thunderstorm cell in this stage is shaped massive or banded, with dense internal structure and clear edges. What is more, the cell's scale is not very large and its reflectivity intensity is not too high but both of which are developing rapidly. The horizontal scale is about 1 km and the vertical scale is slightly larger than the horizontal scale. The reflectivity intensity gradient in the vertical

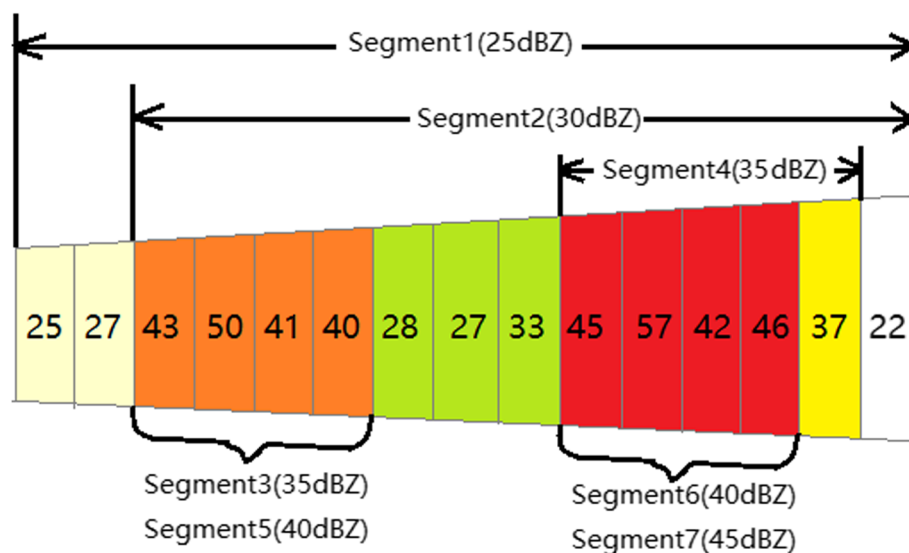
**Fig. 6** Schematic diagram of cell segments

Table 5 Attributes of the cell segment

Attribute	Meaning	Attribute	Meaning
Azimuth (°)	The azimuthal position of a cell segment	Elevation (°)	Angle of the elevation scan
RSbeg (km)	The slant range to the beginning (the front of the first sample volume) of a cell segment	RSend (km)	The slant range to the end (the back of the last sample volume) of a cell segment
MWL (kg/km ²)	Mass weighted length, the mass density-weighted length of a cell segment	MaxRef (dBZ)	The maximum (average) reflectivity factor of a cell segment
MWLS (kg/km)	Mass weighted length squared, the mass density-weighted length squared of a cell segment	Threshold (reflectivity) (dBZ)	The minimum effective reflectivity which the reflectivity factor of a sample volume must meet or exceed to be included in a cell segment

direction is apparent. As for the thunderstorm cell at the maturity stage, it is characterized by the beginning of precipitation and the generation of downward flow with updraft penetrating the cloud column above downward flow (Fig. 5b). Thunderstorm cell at this time is presented as large echo blocks with dense internal structure, clear edges, and locally scattered on plane position display (PPI) image. In addition, the reflectivity intensity is very large, and on the side with a larger gradient, bounded weak echo area, and hook echo can be seen. In the extinction stage, downward flow gradually prevailed and finally completely replaced the updraft (Fig. 5c). Thunderstorm cell in this stage still has a large scale of echo on PPI, but its internal structure is loose and its edge is scattered with continuously decreasing scale and intensity. Besides, the strong echo is mainly distributed in the middle and lower part of the cloud column and its height is continuously decreasing. The echo top is still high, but the reflectivity intensity gradient is obviously decreased.

2.2.2 Thunderstorm identification algorithm

In this paper, a thunderstorm identification algorithm based on SCI algorithm is studied and verified by simulated airborne X-band radar volume scan data. Considering that the threshold of SCI algorithm is proposed based on S-band radar, X-band radar has marked attenuation especially in convective cloud observation [28]. Although the sample volume by sample volume method [32–34] has been made to the correction attenuation of X-band airborne weather radar data in this paper, there still be an insufficient correction. Therefore, seven default reflectivity thresholds are reduced by 5 dBZ. In addition, in order to prevent small thunderstorm cell from being missed, the threshold of the component area is changed from 10 km² to 1 km². The algorithm is carried out according to the steps of cell segment search, cell component search, and storm cell search.

2.2.2.1 Cell segment search Cell segment is defined as a radial sequence of reflectivity by a radial processing technique. These segments are runs of contiguous

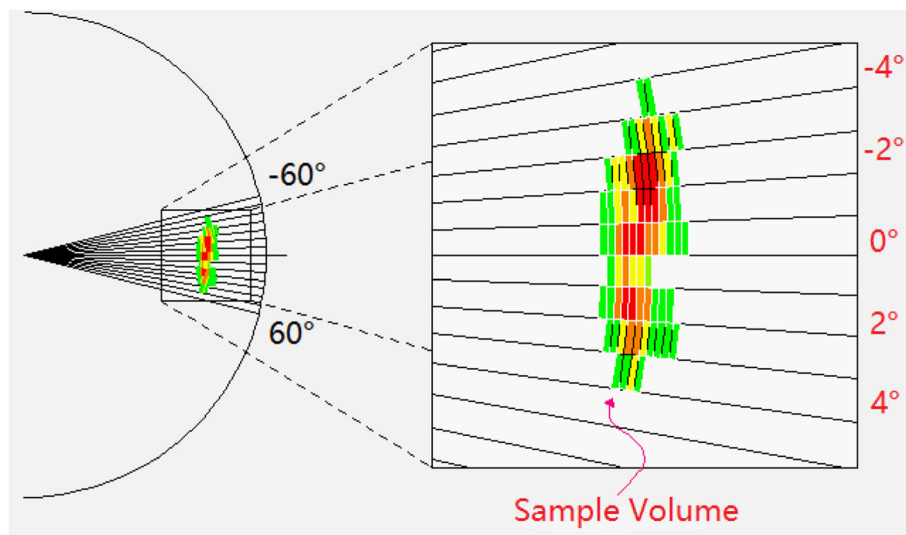
**Fig. 7** Schematic diagram of cell component

Table 6 Thresholds of cell component search

Threshold	Meaning	Default value
Azimuthal separation (°)	The maximum azimuthal separation required for assigning cell segment into the same component	5
Segment overlap (km)	The minimum slant range overlap required for assigning cell segments to the same component	1
Number of segments (unit)	The minimum number of cell segments required in a component	2
Component area (km ²)	A set of required minimum areas for a component. There is an area threshold for each reflectivity threshold used to find cell segments	1

sample volumes with reflectivity values greater than or equal to threshold (reflectivity) and have a combined length greater than threshold (segment length). Also, a segment may contain contiguous sample volumes which are within threshold (dropout reflectivity difference) and whose number should meet threshold (dropout count). In this topic, these thresholds of cell segment search are given in Table 4.

According to the storm cell segment identification parameters in Table 4, Fig. 6 gives an ex-ample of identification results of storm cell segments.

Each identified cell segment has the following attributes in Table 5.

According to the position and intensity of the reflectivity factor contained in each segment, MWL and MWLS of the storm cell segment are calculated by Eqs. (5) and (6).

$$MWL = \sum_k \left[53000 \left(\frac{10^{\frac{dBZE}{10}}}{486} \right)^{\frac{1}{1.37}} R_k \right] \quad (5)$$

$$MWLS = \sum_k \left[53000 \left(\frac{10^{\frac{dBZE}{10}}}{486} \right)^{\frac{1}{1.37}} R_k^2 \right] \quad (6)$$

Here, dBZE is the reflectivity factor of a sample volume, R_k is the slant range from radar to the center of a sample volume.

2.2.2.2 Cell component search Cell component is a sector set of segments in an elevation scan (Fig. 7). All identified cell segments are traversed in sequence according to seven default reflectivity thresholds. The first segment traversed is taken as the beginning segment of a cell component. And if the next segment meets threshold (azimuthal separation) and threshold (segment overlap), it will be merged into the component and taken as the ending segment of the component. Continuing to process other segments in this way, every time a segment is newly added, this segment replaces to be the ending segment of the current component. This component search does not end until a segment that does not meet the thresholds appears, and it is used as the beginning segment of the next cell component search. When all cell segments are traversed, the cell component search is completed. Finally, retain the cell components that meet threshold (number of segments) and threshold (component area) at the same time. The values of threshold parameters in the cell component search are shown in Table 6.

Each identified cell component has the following attributes in Table 7.

Based on the attributes of segments contained, the MC of a component can be calculated by Eq. (7).

$$MC = \sum_{i=1}^n \left[(MWL_i)(SVL) \left(\text{DELAZ}_{avg_j} \right) (\pi/180)/10^6 \right] \quad (7)$$

Where, i is an index of cell segments in a storm component, a total of n . And j is an index of the elevation

Table 7 Attributes of cell component

Attribute	Meaning	Attribute	Meaning
EL (°)	The elevation angle of an elevation scan	MC(kg/km)	The mass-weighted area of a component
AC (°)	The azimuth of the mass-weighted center of a component	DBZECmax(dBZ)	The maximum reflectivity factor in a component
RC (km)	The slant range to the mass-weighted center of a component	ACbeg(°)	The most counterclockwise extent of a component
XC (km)	The (flat earth projected) x-coordinate of the centroid of a component	ACend(°)	The most clockwise extent of a component
YC (km)	The (flat earth projected) y-coordinate of the centroid of a component	RCbeg(km)	The (flat earth projected) range of the closest part of a component (to the radar)
HC (km)	The height above ground (of the mass-weighted center) of a component	RCend(km)	The slant range of the farthest part of a component (from the radar)

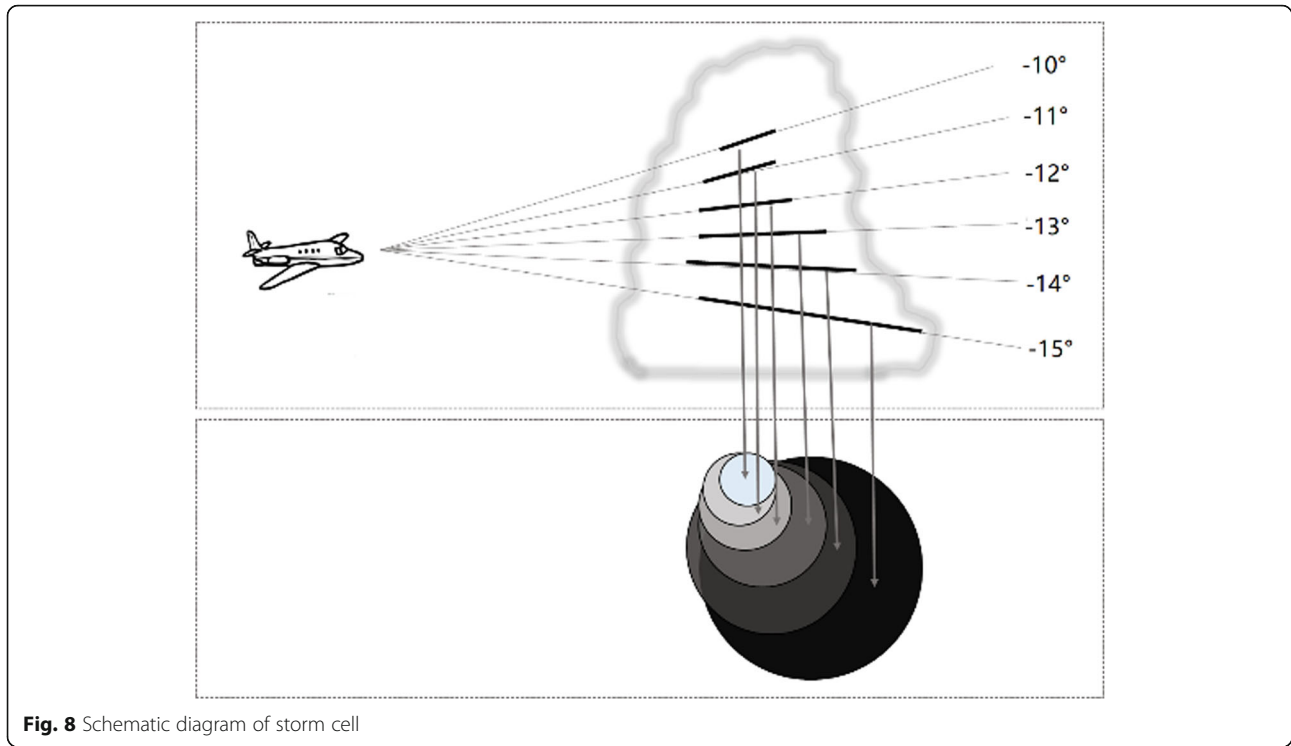


Fig. 8 Schematic diagram of storm cell

scan at which the cell segment is located. SVL is the range of sample volume (0.1 km in this paper). And $DELAZ_{avg}$ is the average azimuth in an elevation scan, the average difference in horizontal azimuthal position of the adjacent radials (1° in this paper). The centroid, called the mass-weighted center as well, of a component can be calculated based on MC by Eqs. (8) and (9).

$$XC = \sum_{i=1}^n \left[\frac{\sin(AC_i)(MWLS_i)(SVL)(DELAZ_{avg_j})}{\cos(EL_j)(\pi/180)/10^6} \right] / MC \quad (8)$$

$$YC = \sum_{i=1}^n \left[\frac{\cos(AC_i)(MWLS_i)(SVL)(DELAZ_{avg_j})}{\cos(EL_j)(\pi/180)/10^6} \right] / MC \quad (9)$$

XC and YC are the x -coordinate and y -coordinate, respectively, of the cell centroid components. The cell components included in each elevation are identified by seven default thresholds. If the centroid of a cell component with a larger reflectivity threshold is within the one with a smaller reflectivity threshold, the smaller one will be discarded and only the larger one is retained.

2.2.2.3 Storm cell search A storm cell is formed by the components vertically correlated (Fig. 8). Starting

from the lowest elevation, the centroid of the components at adjacent elevation scans are compared in the horizontal plane. All the components included in an elevation scan are sorted by decreasing mass and the largest one is compared first. For each component in the current elevation scan, the distance between the center of every component in the next elevation scan and that of this component is compared according to three specified search radii (set as 5 km, 7.5 km, and 10 km) in turn. Similarly, the comparison is carried out on every component of each elevation angle and the component of the next elevation. The correlated storm components are combined to form a three-dimensional storm cell which has the attributes in Table 8.

In addition, some important attributes are described in detail as follows:

- (a) The centroid position of storm cell

Firstly, calculate the MSV (mass-weighted volume) of storm cell by Eq. (10).

$$MSV = \sum_{k=1}^n [MC_k \cdot DCH_k] \quad (10)$$

Where n is the total number of components included in a storm cell and k is the index, DCH is the height of

Table 8 Attributes of storm cell

Attribute	Meaning	Attribute	Meaning
NC (unit)	The number of components in a storm cell	VIL (kg/km ²)	The vertically integrated liquid
AS (°)	The azimuth of the centroid (or mass-weighted center) of a storm cell	TOP (km)	The height of the highest component in a storm cell
RS (km)	The (flat earth projected) range of the centroid of a storm cell	BASE (km)	The height of the lowest component in a storm cell
XSC (km)	The (flat earth projected) x-coordinate of the centroid of a storm cell	LOWEL (°)	The elevation angle of the lowest component in a storm cell
YSC (km)	The (flat earth projected) y-coordinate of the centroid of a storm cell	HIGHEL (°)	The elevation angle of the highest component in a storm cell
HSC (km)	The height of the centroid of a storm cell	MSV (kg)	The mass-weighted volume of a storm cell
ZMAX (dBZ)	The maximum reflectivity factor (component) of the component s in a storm cell	BEGAZI (°)	The azimuth of the first cell segment of a storm cell
HZMAX (km)	The height above ground of the sample volume corresponding to ZMAX	ENDAZI (°)	The azimuth of the last cell segment of a storm cell
BEGRAN (km)	The range(slant) to the front (closest to the radar) of the first sample volume of a cell segment	ENDRAN (km)	The ending range(component), the slant range of the farthest part of a component (from the radar)

the storm component. Based on MSV, the coordinates of the storm cell's centroid can be further obtained by Eqs. (11) and (12) as follows:

$$XSC = \frac{\sum_{k=1}^n [XC_k \cdot MC_k \cdot DCH_k]}{MSV} \quad (11)$$

$$YSC = \frac{\sum_{k=1}^n [YC_k \cdot MC_k \cdot DCH_k]}{MSV} \quad (12)$$

XSC and YSC are the x -coordinate and y -coordinate of the storm cell centroid.

(b) Top

The height of the highest component in a storm cell. Traversing all the segments of the last component in the storm call, the height of the mass weight center of the

last cell segment of the component is the top height of the storm cell.

(c) Base

The height of the lowest component in a storm cell. Traversing all the segments of the first component in the storm call, the height of the mass weight center of the first cell segment of the component is the bottom height of the storm cell.

(d) ZMAX and HZMAX

Traversing all reflectivity factor of the storm cell and taking the maximum value of dBZ and the height thereof as the ZMAX and HZMAX, respectively.

(e) VIL

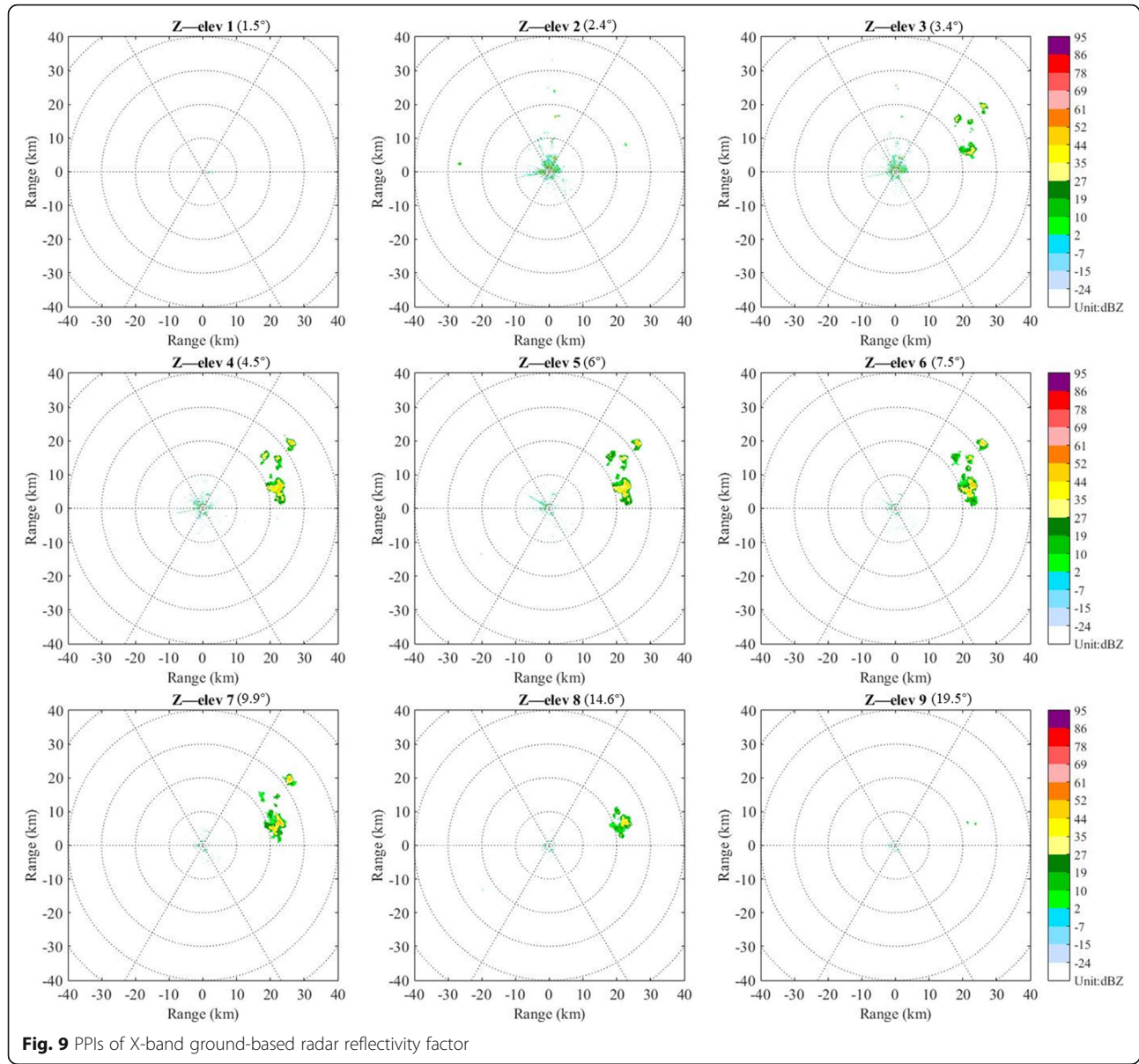
The VIL (vertically integrated liquid) can be calculated by Eq. (13) as follows:

Table 9 Thresholds of storm cell merge

Threshold	Meaning	Default value
Elevation merge(°)	The maximum difference in the elevation angles between the top of one storm cell and the bottom of another storm cell required to merge the storm cells	3
Horizontal merge(km)	The maximum horizontal distance between two centroids required to merge the storm cells	8
Height merge(km)	The maximum difference in the height between the top of one storm cell and the bottom of another storm cell required to merge the storm cells	4

Table 10 Thresholds of storm cell deletion

Threshold	Meaning	Default value
Horizontal delete (km)	The maximum horizontal distance between two centroids required to delete one of the storm cells	5
Depth delete (km)	The maximum difference in the depths of two storm cells required to delete one of the storm cells	4



$$VIL = 3.44 \times 10^{-3} \sum_{i=1}^{N-1} \left(\frac{Z_i + Z_{i+1}}{2} \right)^{\frac{4}{3}} \Delta h_i \quad (13)$$

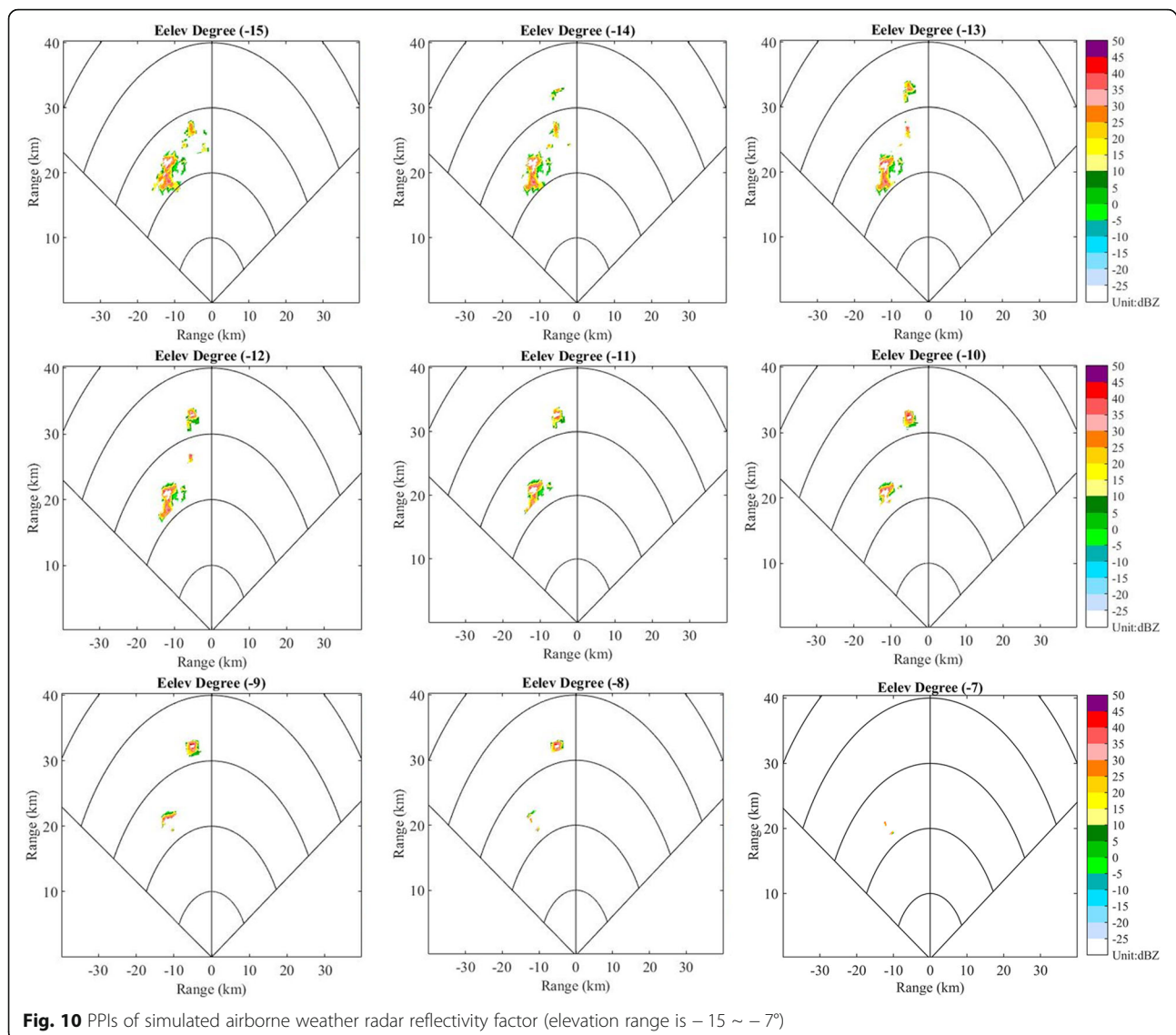
Here, N is the total number of components in a storm cell, and i is the index, Z_i means $DBZEC_{max}$, is the maximum reflectivity factor of the component. Δh_i is the height difference between two components in adjacent elevation scans of component i . In this paper, when calculating, the maximum threshold value of reflectivity factor is set to 56 dBZ (adjustable). That is, those with intensity below 56 dBZ are treated as liquid water, and those above 56 dBZ are calculated as 56 dBZ.

Traversing all the identified storm cells, if two storm cells have no cell components existing in a common elevation scan and meet the threshold shown in Table 9 at the same time, they can be combined into one storm cell.

When two adjacent storm cells satisfy any threshold in Table 10 below, the storm cell with smaller VIL in the two storm cells will be deleted.

3 Results and discussions

Thunderstorm identification results of airborne weather radar data simulated by X-band ground-based radar data at 04:58 UTC on July 20, 2010, are taken as an example

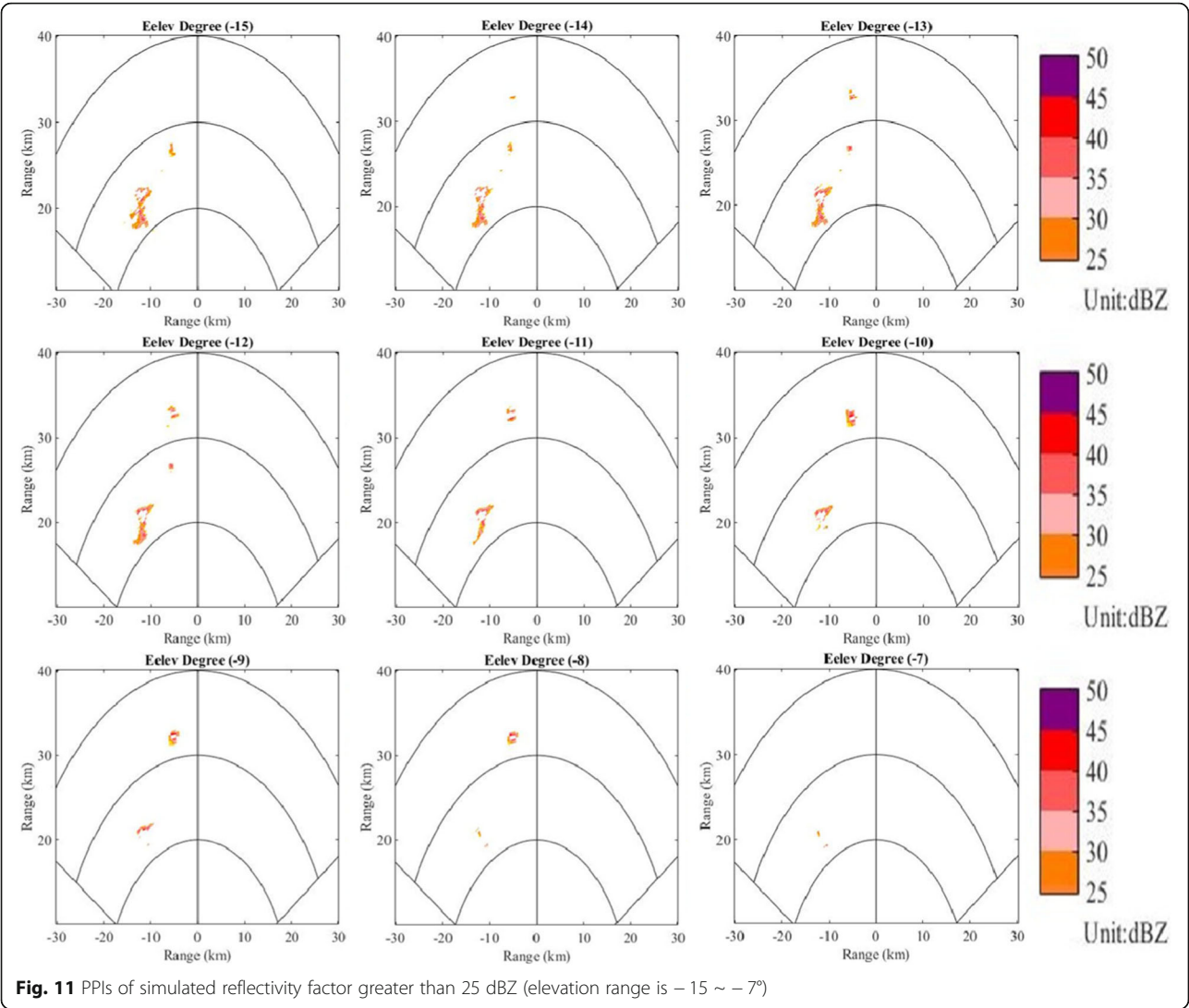


for analysis. The PPIs of X-band radar reflectivity factor images are shown in Fig. 9. The simulation results after attenuation correction are shown in Fig. 10 (only ground-based radar data from 0 to 120° are used). And Fig. 11 is the retention of more than 25 dBZ based on Fig. 10.

At the range of 20~30 km in the elevation scan of -15° , there are two areas of reflectivity factor greater than 25 dBZ (Fig. 11). The one near 30 km is very small and decreasing along with the elevation angle increasing, which will not be identified as a thunderstorm cell for that it cannot meet the threshold (component area). However, the other one near 20 km has enough echo in elevations from -15° to -9° with high reflectivity factor so that it can be considered as a thunderstorm cell. What's more, as the elevation angle

increases, an echo region appears at the range of 30~40 km with high reflectivity and gets clearer from -14° to -8° , which may be another thunderstorm. In addition, there are some no-echo areas in these two areas in some elevation scans, which should be caused by serious attenuation of X-band radar echo to strong convection. These no-echo areas may be the strong echo center of thunderstorm cells. To sum up, there may be two thunderstorm cells here, one located at the range of 20~30 km and the azimuth of -30° or so. Another is located at the range of 30~40 km and the azimuth of -10° approximately.

After using the thunderstorm identification algorithm, two thunderstorm cells are identified and their attributes are shown in Table 11. The attributes of the components contained in thunderstorm cell 1 (thunderstorm cell whose serial number is 1 in Table 11) and thunderstorm 2



(thunderstorm cell whose serial number is 2 in Table 11) are showing in Tables 12 and 13, respectively.

From the last two tables above, thunderstorm 1 contains seven cell components. Since the strong echo region corresponding to this thunderstorm is already very small when the elevation angle reaches -8° , the component no longer exists above -8° . Thunderstorm 2 contains four components that exist in the elevation from -12° to -9° . This result is consistent with the echo image in Figs. 10 and 11.

According to the attributes including EL, ACbeg, ACend, RCbeg, and RCend of the components contained in each thunderstorm cell, the position of these components is drawn on the echo map of reflectivity factor retaining more

Table 11 Attributes of thunderstorm cells

Serial number									
	NC (unit)	AS ($^\circ$)	RS (km)	XSC (km)	YSC (km)	HSC (km)	ZMAX (dBZ)	HZMAX (km)	VIL (kg/km^2)
1	7	-29.83	23.62	-11.75	20.49	2.72	54.5	4.74	27.66
2	4	-9.74	32.24	-5.45	31.77	4.27	51.00	3.32	4.35
	MSV (kg)	TOP (km)	BASE (km)	LOWEL ($^\circ$)	HIGHEL ($^\circ$)	BEGAZI ($^\circ$)	ENDAZI ($^\circ$)	BEGRAN (km)	ENDRAN (km)
1	16.47	6.33	3.89	-15	-9	-32	-27	22.45	25.65
2	3.00	5.05	3.32	-12	-9	-10	-8	31.55	34.25

Table 12 Attributes of cell components included in thunderstorm 1

Comp	EL (°)	AC (°)	RC (km)	XC (km)	YC (km)	HC (km)	DBZECmax (dBZ)	MC (kg/km)	ACbeg (°)	ACend (°)	RCbeg (km)	RCend (km)
1	-15	-29.66	23.76	-11.75	20.64	3.89	51.5	1.94	-30	-28	23.55	25.65
2	-14	-29.30	23.52	-11.51	20.51	4.35	52.5	3.62	-30	-27	22.75	25.45
3	-13	-30.01	23.53	-11.77	20.37	4.74	54.5	3.84	-31	-28	22.65	25.35
4	-12	-30.02	23.43	-11.72	20.29	5.16	54.5	3.66	-31	-28	22.45	25.05
5	-11	-30.02	23.43	-11.72	20.29	5.56	54.5	3.63	-31	-28	22.45	24.95
6	-10	-30.01	23.44	-11.72	20.30	5.97	54.0	3.55	-31	-28	22.65	24.85
7	-9	-30.97	23.69	-12.19	20.32	6.33	54.5	2.87	-32	-29	23.55	24.85

than 25 dBZ. And cell components corresponding to thunderstorm 1 and thunderstorm 2 are represented in red and blue respectively (Fig. 12).

Combining tables and figures above, it can be found that thunderstorm 1 has the following characteristics. As Fig. 12 shows, the echo block area is large with a clear edge, and its internal structure is compact with local scatter. According to Table 12, the DBZECmax of every component is above 50 dBZ and those at the middle-high part are close to 55 dBZ, indicating that strong convection exists. All the MC values are high and have the distribution characteristics of small bottom and large middle-high part, indicating the simultaneous existence of updraft and downward flow. And we can see from Table 11, the BASE is about 3.8 km and the TOP is about 6.3 km, so thunderstorm 1 has a certain vertical spatial scale. The VIL value of thunderstorm 1 is 33.36 kg/km², which has abundant liquid water content and may cause dangerous weather such as precipitation, hail, and thunderstorm gale. In summary, thunderstorm 1 is in the mature stage, so the aircraft should avoid in time during flying.

Meanwhile, characteristics of thunderstorm 2 also can be found from these tables and figures. The radar echo is blocky shape in Fig. 12, with dense internal structure and clear edges, is obviously smaller than thunderstorm cell 1. The horizontal scale is small and the vertical scale is about 1.7 km, slightly larger than the horizontal scale, which can be evidenced by the BASE and the TOP in Table 11 and the MC in Table 13. Besides, the MC values of all the components

present a tower-like feature, indicating that updraft flow exists mainly at this moment. The maximum reflectivity factor is high as the DBZECmax of all components is nearly 50 dBZ. What can be found more from Table 11 is that the VIL value of the thunderstorm 2 is 7.14 kg/km², which is a good instruction for that there has accumulated a certain liquid water content. If it continues to develop, it will be a mature thunderstorm and some weather phenomena such as precipitation will occur. To sum up, thunderstorm 2 is in the development stage, so the aircraft should pay attention to its development and defense in time.

Because cell components with smaller reflectivity factor threshold are discarded and only components with larger threshold are retained during the identification process, the marked component area does not include all the reflectivity factors larger than 25 dBZ. However, the no-echo area that thought to be the strong echo center of storm cells mentioned earlier in this section falls in the middle of the marked component area in Fig. 12. In addition, the SCI algorithm was originally used to identify the centroid of the storm cell. So this consistency verifies that the thunderstorm identification algorithm is workable.

Finally, from Fig. 13 where are the PPIs of the S-band radar reflectivity factor at 05:00 UTC closest to the time of the X-band data, it can be found that there is an area of strong echo in 20~30 km marked by red circles. There are obvious distributions at 9 elevation angles. And from the PPI of 10.0° elevation, it can be seen that the maximum reflectivity is above

Table 13 Attributes of cell components included in thunderstorm 2

Comp	EL (°)	AC (°)	RC (km)	XC (km)	YC (km)	HC (km)	DBZECmax (dBZ)	MC (kg/km)	ACbeg (°)	ACend (°)	RCbeg (km)	RCend (km)
1	-12	-9.78	32.44	-5.51	31.97	3.32	51.0	1.15	-10	-8	32.55	34.25
2	-11	-9.89	32.36	-5.56	31.88	3.89	49.5	1.01	-10	-8	32.15	33.95
3	-10	-9.72	32.18	-5.43	31.72	4.48	49.5	1.62	-10	-8	31.65	33.65
4	-9	-9.63	32.05	-5.36	31.60	5.05	49.5	1.44	-10	-8	31.55	33.35

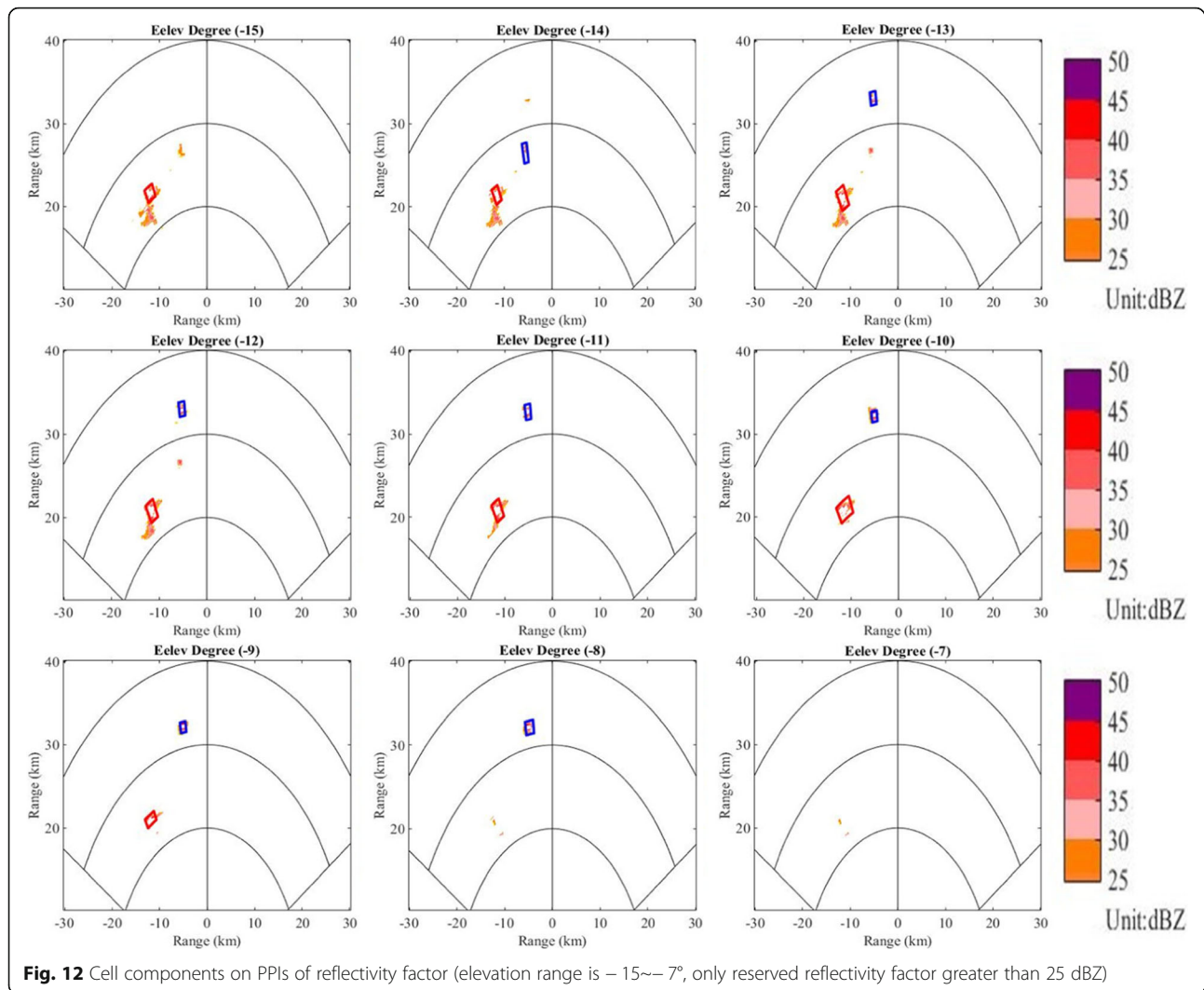


Fig. 12 Cell components on PPIs of reflectivity factor (elevation range is -15° to -7° , only reserved reflectivity factor greater than 25 dBZ)

50 dBZ, indicating that this area is a thunderstorm cell in the mature stage. Not far from 30 km, there is a smaller strong echo area marked by blue circles and it is obviously distributed at 6 elevations from 1.6° to 10° . It can be seen from the PPIs of elevations 1.4° to 4.4° that the maximum reflectivity is between 45 dBZ and 50 dBZ, indicating that it is a relatively small-scale thunderstorm. Since the S-band and X-band radar positions are only about 2 km away, there is a small gap in the echo position. But in general, this is consistent with the thunderstorm identification result obtained by algorithm proposed in this paper, which can further verify the correctness of the result and the reliability of the algorithm.

4 Conclusion

In this paper, by preset detection parameters of airborne weather radar, an airborne weather radar simulation model of reflectivity volume scan data is

established. Using X-band ground-based weather radar volume scan data as the simulation data source, the reflectivity volume scan data of simulated airborne weather radar is obtained by interpolation and calculation. Considering the attenuation of X-band Radar and the characteristics of thunderstorm cells, this paper studies a thunderstorm identification algorithm for the simulated airborne radar based on SCI algorithm and gives an example of thunderstorm identification. By analyzing the identified results and comprising with S-band radar data, it shows that the algorithm can effectively identify the thunderstorm cell in the sector scanning area in front of the plane, including not only the mature thunderstorm cell, but also those in the development stage with a certain scale. The algorithm also outputs some attributes of identified thunderstorm cells, including centroid position, the top height, the bottom height, VIL, et al., which is of guiding significance for aircraft flight avoidance and verifies the

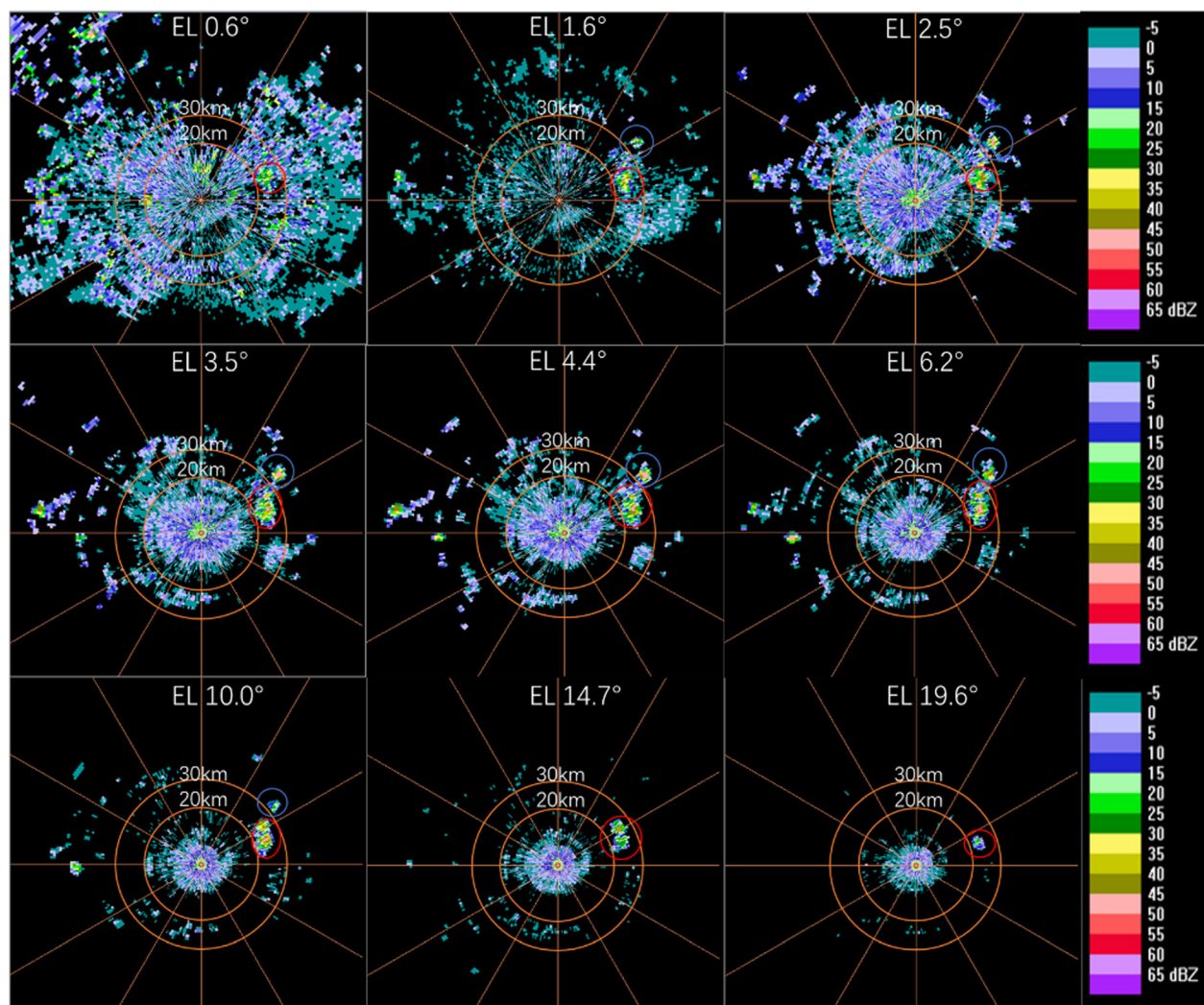


Fig. 13 PPIs of S-band radar reflectivity factor at 05:00 UTC on July 7, 2010

feasibility of the simulated airborne weather radar volume scan data simultaneously.

However, this algorithm also lost a lot of information in the process of identification. As a result, it cannot show a complete figure of components very well. Only the location of thunderstorm centroid identified by SCI in the flight process is not conducive to judging the specific safe distance. And the experiment did not consider the influence of aircraft's moving speed on radar detection data, so it has certain limitations.

Abbreviations

3D: Three-dimensional; CINRAD: New Generation of Doppler Weather Radar in China; PPI: Plane Position Indication; SCI: Storm cell identification; TITAN: Thunderstorm Identification, Tracking, Analysis, and Now Casting; WMO: World Meteorological Organization

Authors' contributions

XW and RL proposed the airborne radar scan mode and study the thunderstorm identification algorithm. JL wrote the thunderstorm

identification code and carried out identification experiments. JXH established the data transform model from ground-based to the airborne radar. GQW and ZLX conducted the X-band airborne weather radar data simulation. HJW analyzed the thunderstorm identification performance and improved the identification program. All authors read and approved the final manuscript.

Funding

This research was funded by National Natural Science Foundation of China (award number U1733103), the National Key R&D Program of China (award number 2018YFC 1506104), Department of Science and Technology of Sichuan Province (award numbers 2018JZ0030 and 2019YJ0316), and Chengdu Science and Technology Bureau (award number 2016-XT00-00015-GX).

Availability of data and materials

The datasets supporting the conclusions of this article are private, and it came from the CMA Key Laboratory of Atmospheric Sounding, Chengdu, Sichuan, China.

Competing interests

The authors declare that they have no competing interests.

Author details

¹Key Laboratory of Atmospheric Sounding of China Meteorological Administration, Electronic Engineering College of Chengdu University of Information Technology, Chengdu 610225, Sichuan, China. ²The Second Research Institute of CAAC, Chengdu 610041, Sichuan, China.

Received: 21 November 2019 Accepted: 16 January 2020

Published online: 10 February 2020

References

1. L. He, *Research on Signal Processing Technology of Beam Multi-Scan Airborne Weather Radar*[D] (Nanjing University of Aeronautics and Astronautics, 2014)
2. Y. Gao, *Research on Key Technologies of Airborne Weather Radar Detection System*[D] (Beijing University of Posts and Telecommunications, 2009)
3. X. Yu, X. Zhou, X. Yu, Progress of Thunderstorm and Severe Convection Near Weather Forecast Technology[J]. *Acta Meteorologica Sinica* **70**(03), 311–337 (2012)
4. X. Wei, H. Jiang, G. Wang, et al., Disaster Analysis of Thunderstorm to Aviation Flight[J]. *Meteorology Journal of Inner Mongolia* **4**, 42–44 (2013)
5. X. Zhang, Analysis and identification of thunderstorm weather and its impact on flight[J]. *Journal of Changsha Aeronautical Vocational and Technical College* **11**(2), 49–54 (2011)
6. M. Dixon, G. Wiener, TITAN: Thunderstorm identification, tracking, analysis, and nowcasting—A radar-based methodology[J]. *J. Atmos. Ocean. Technol.* **10**(6), 785–797 (1993)
7. L. Han, S. Fu, L. Zhao, et al., 3D convective storm identification, tracking, and forecasting—An enhanced TITAN algorithm[J]. *J. Atmos. Ocean. Technol.* **26**(4), 719–732 (2009)
8. L. Wang, X. Liu, M. Wei, Simulation of adaptive hazard the weather warning method for airborne weather radar[J]. *Journal of System Simulation* **29**(07), 1572–1581 (2017)
9. H. Kyznarová, P. Novák, CELLTRACK—Convective cell tracking algorithm and its use for deriving life cycle characteristics[J]. *Atmos. Res.* **93**(1), 317–327 (2009)
10. J.T. Johnson, P.L. Mac Keen, A. Witt, et al., The storm cell identification and tracking algorithm: An enhanced WSR-88D algorithm[J]. *Weather Forecast.* **13**(2), 263–276 (1998)
11. V. Lakshmanan, K. Hondl, R. Rabin, An efficient, general-purpose technique for identifying storm cells in geospatial images[J]. *J. Atmos. Ocean. Technol.* **26**(3), 523–537 (2009)
12. J. Choi, F. Olivera, S.A. Socolofsky, Storm identification and tracking algorithm for modeling of rainfall fields using 1-h NEXRAD rainfall data in Texas[J]. *J. Hydrol. Eng.* **14**(7), 721–730 (2009)
13. V. Lakshmanan, R. Rabin, V. De Brunner, Multiscale storm identification and forecast[J]. *Atmos. Res.* **67**, 367–380 (2003)
14. L. Han, J. Sun, W. Zhang, et al., A machine learning nowcasting method based on real-time reanalysis data[J]. *J. Geophys. Res.-Atmos.* **122**(7), 4038–4051 (2017)
15. J. Liang, X. Yu, H. Li, Collaborative Energy-Efficient Moving in Internet of Things: Genetic Fuzzy Tree vs. Neural Networks[J]. *IEEE Internet Things J.* **6**, 6070–6078 (2019)
16. X. Yu, J. Liang, Genetic fuzzy tree based node moving strategy of target tracking in multimodal wireless sensor network[J]. *IEEE Access* **6**, 25764–25772 (2018)
17. J. Liang, C. Mao, Distributed Compressive Sensing in Heterogeneous Sensor Network[J]. *Signal Processing(Elsevier)* **126**, 96–102 (2016)
18. B. Dolan, S.A. Rutledge, A theory-based hydrometeor identification algorithm for X-band polarimetric radars[J]. *J. Atmos. Ocean. Technol.* **26**(10), 2071–2088 (2008)
19. J. Cao, L. Liu, R. Ge, Research on Fuzzy Logic Method in Identifying Precipitation Particle Phase States by Dual-Line Polarization Radar [J]. *Atmos. Sci.* **29**(5), 827–836 (2005)
20. Y. Liu, H. Xiao, Z. Yao, et al., Phase identification of condensate particles in clouds by X-band dual polarization radar [C]. *Annual Meeting of China Meteorological Society*, 925–936 (2014)
21. J. Liang, X. Liu, K. Liao, Soil moisture retrieval using UWB echoes via fuzzy logic and machine learning[J]. *IEEE Internet Things J.* **5**, 3344–3352 (2017)
22. J. Liang, F. Zhu, Soil Moisture Retrieval From UWB Sensor Data By Leveraging Fuzzy Logic[J]. *IEEE Access* **6**, 29846–29857 (2018)
23. L. Huang, *Recognition algorithm and implementation of severe convective weather based on radar data*[D] (Nanjing University of Information Science and Technology, 2012)
24. D. Lu, *Storm identification, tracking design and hail cloud radar echo characteristics analysis in Jianghuai Region based on SCIT Algorithm*[D] (Nanjing University of Information Science and Technology, 2015)
25. Y. Duan, Y. Xu, S. Zhi, Application analysis of improved scit algorithm in hail suppression operation[J]. *Meteorology and Disaster Reduction Research* **37**(04), 42–49 (2014)
26. L. Han, H. Wang, X. Tan, et al., Research progress of storm identification, tracking and early warning based on radar data[J]. *Meteorological Monthly* **01**, 3–10 (2007)
27. F. Li, B. Li, L. Wu, et al., An introduction of WMO 8th radiosondes inter-comparison and integrated remote instruments experiment[J]. *Adv. Earth Science* **27**(8), 916–924 (2012)
28. B. Lv, S. Yang, J. Wang, et al., Data Quality Evaluation of X-Band Dual-Line Polarization Doppler Radar[J]. *Journal of Arid Meteorology* **34**(6), 1054–1063 (2016)
29. Y. Huang, Y. Zhang, Comparative Study on Data Interpolation Methods of Doppler Weather Radar [J]. *Remote sensing information* **02**, 40–46 (2008)
30. Jr, B. R. R. B. Thunderstorm structure and circulation[J]. *J. Meteorol.*, 1948,5(6), 71–86.
31. X. Yu, Principle and operational application of doppler weather radar [M] (China Meteorological Press, 2006).
32. P. Zhang, Z. Wang, Research on correction algorithm of weather radar echo attenuation part I: theoretical analysis [J]. *Plateau Meteorology* **V20**(1), 1–5 (2001).
33. Z. Wang, P. Zhang, Research on correction algorithm of weather radar echo attenuation part II: numerical simulation and case study [J]. *Plateau Meteorology* **20**(2), 115–120 (2001).
34. C. Wang, X. Hou, X. Li, et al., Correction of Ka-band cloud radar reflectance factor attenuation based on hierarchical library-by-library method[J]. *Journal of Chengdu University of Information Technology* **31**(4), 358–362 (2016).

Publisher's Note

Springer Nature remains neutral with regard to jurisdictional claims in published maps and institutional affiliations.

Submit your manuscript to a SpringerOpen[®] journal and benefit from:

- Convenient online submission
- Rigorous peer review
- Open access: articles freely available online
- High visibility within the field
- Retaining the copyright to your article

Submit your next manuscript at ► [springeropen.com](https://www.springeropen.com)